

# Reverse bias breakdown and photocurrent gain in $\text{CH}_3\text{NH}_3\text{PbBr}_3$ films

Cite as: Appl. Phys. Lett. **120**, 113505 (2022); doi: [10.1063/5.0082425](https://doi.org/10.1063/5.0082425)

Submitted: 15 December 2021 · Accepted: 7 March 2022 ·

Published Online: 16 March 2022



View Online



Export Citation



CrossMark

M. Auf der Maur,<sup>1,a)</sup> F. Matteocci,<sup>1</sup> A. Di Carlo,<sup>1,2</sup> and M. Testa<sup>3</sup>

## AFFILIATIONS

<sup>1</sup> CHOSE (Centre for Hybrid and Organic Solar Energy), Department of Electronic Engineering, University of Rome "Tor Vergata," 00133 Rome, Italy

<sup>2</sup> CNR-ISM, Via del Fosso del Cavaliere 100, 00133 Rome, Italy

<sup>3</sup> INFN Laboratori Nazionali di Frascati, Via Enrico Fermi 54, 00044 Frascati, Italy

<sup>a)</sup> Author to whom correspondence should be addressed: [auf.der.maur@ing.uniroma2.it](mailto:auf.der.maur@ing.uniroma2.it)

## ABSTRACT

Perovskite films are promising candidates for fast, sensitive, and large area photodetectors. A gain in perovskite based detectors has been observed in several architectures, but a model describing the underlying mechanism is still missing or at least incomplete. Here, we present measurements of  $\text{CH}_3\text{NH}_3\text{PbBr}_3$  films under reverse bias exhibiting breakdown at 4–5 V and small photocurrent gain  $\leq 2$ , which based on a phenomenological model, we explain tentatively by tunnel-assisted injection from the  $\text{TiO}_2$  electron transport layer and carrier multiplication, mediated by the electric field due to mobile ions.

Published under an exclusive license by AIP Publishing. <https://doi.org/10.1063/5.0082425>

During the last decade, an extensive research and development effort has been spent on perovskite based detectors for visible light.<sup>1,2</sup> High sensitivity has been demonstrated in such devices, and in several cases, a photocurrent gain has been observed,<sup>3–12</sup> meaning that the number of extracted carriers is larger than the absorbed number of photons per unit time. Perovskite detectors with various device architectures have shown gain, accompanied, to date, by a time response slower than  $\sim 1 \mu\text{s}$ . Gains between 150 and 2400 have been observed in vertical devices, based either on  $\text{CH}_3\text{NH}_3\text{PbI}_3$  or  $\text{CH}_3\text{NH}_3\text{PbBr}_3$  perovskites, using a mesoporous  $\text{TiO}_2$  layer,<sup>3,6</sup> or compact thin  $\text{TiO}_2$  layers<sup>8</sup> as hole blocking layers (HBL), or not using any HBL at all.<sup>3</sup> Some authors report vertical architectures specifically designed to include interface trap states.<sup>7</sup> Also, vertical devices with Au contacts directly deposited on the two faces of a  $\text{CsPbBr}_3$  single crystal have shown gain.<sup>12</sup> The smallest rise and fall times among the above vertical architectures were between 5.7 and 41  $\mu\text{s}$ .<sup>7</sup>

Lateral devices using metal contacts directly deposited on the perovskite<sup>4,5,9–11</sup> have shown gain up to  $\sim 2000$ ,<sup>5,9</sup> with the smallest rise and fall times being 20 and 39  $\mu\text{s}$ , respectively.<sup>9</sup>

The underlying physical mechanisms of the observed gain have not been fully understood in all cases. This is partly due to the peculiarity of halide perovskites in which beside electrons and holes also ions may take part in the conduction mechanism. A model based on ion migration was proposed to explain the observed gain, e.g., by

Domanski *et al.*<sup>6</sup> Some structures work as photoresistor, where the incident light increases the conductivity of the active layer,<sup>9</sup> while others are believed to be governed by the modification of a carrier injection barrier at one of the perovskite interfaces, due to charge accumulation or trapping.<sup>7</sup>

The presence of gain in a photodetector is critical to achieve high sensitivity, which is of special importance in applications working at low light intensities. Also, fast time response is important in many cases. Silicon avalanche photodiodes (APD) and silicon photon multiplier devices (SiPM) are well established and widely used in detector applications with the above requirements. Their working principle is based on avalanche multiplication,<sup>13</sup> where the high electric field under reverse bias allows to accelerate charge carriers to a sufficiently high energy to initiate impact ionization, thus generating additional electron–hole pairs. Successive ionizations can happen depending on the active layer thickness and electric field, giving eventually rise to an avalanche and an associated potentially large gain.

Impact ionization so far has not been considered in the literature as a possible co-mechanism to interpret the observed gain, neither on its own nor eventually masked by the mechanisms described above. Carrier multiplication has been observed, however, in  $\text{CsPbI}_3$  perovskite nanocrystals.<sup>14</sup> It has also been argued<sup>15</sup> that methylammonium lead halide perovskites fulfill criteria that enable multi-carrier generation through impact ionization. Also, an ionic avalanche-like

mechanism has been proposed recently to explain the observation of persistent photocurrent in  $\text{MAPbI}_3$ .<sup>16</sup>

In order to understand whether impact ionization and avalanche multiplication could be observed in lead halide perovskites, we have studied methylammonium lead bromide ( $\text{CH}_3\text{NH}_3\text{PbBr}_3$ , referred to as  $\text{MAPbBr}_3$  in the following) thin film devices<sup>17</sup> deposited on mesoporous- $\text{TiO}_2$ /compact- $\text{TiO}_2$ /FTO/glass substrates. We used laser etched Fluorine-doped Tin Oxide (FTO) glass substrates (Pilkington) as transparent conductive substrates for the fabrication of four-pixel devices. The FTO glass substrates are cleaned in an ultrasonic bath using acetone and 2-propanol for 10 min each. A 30 nm thick compact  $\text{TiO}_2$  layer is deposited using spray-pyrolysis technique at 460 °C. Then, diluted  $\text{TiO}_2$  paste (30NR-D, Greatcell Materials) in ethanol (1:5 w/w) is deposited by spin coating to obtain a 220 nm thick mesoporous  $\text{TiO}_2$  layer. After that, the samples are soaked for 10 min under UV lamp to improve the surface wettability. Perovskite solution is prepared by mixing  $\text{MABr}$  (Greatcell Materials) and  $\text{PbBr}_2$  (TCI chemicals) precursors in dimethyl sulfoxide with 1.4 M concentration. The perovskite film is deposited by spin coating at 4000 rpm for 20 s using a solvent quenching method. Toluene is deposited as anti-solvent after 10 s. Then, the perovskite films are annealed at 80 °C for 10 min. Additionally, the obtained 300 nm thick films are recrystallized by exposure to methylamine gas for 1–2 s in air and annealed at 80 °C to remove any by-product of the reaction. Finally, 80 nm thick Au electrodes are thermally evaporated at rate of 0.3 Å/s for the first 10 nm and then increased to 1 Å/s. A photograph of the measured device is shown in Fig. 1(a).

The devices have been characterized under reverse bias up to  $-6$  V, in the dark and under white light with intensity of  $\sim 0.25$  suns. From the measured current, we calculated the photocurrent gain as

$$G(V) = \frac{I_{\text{light}}(V) - I_{\text{dark}}(V)}{I_{\text{light}}(V_{\text{ref}}) - I_{\text{dark}}(V_{\text{ref}})}, \quad (1)$$

where  $V_{\text{ref}}$  is a reference voltage at which the current is assumed to be purely photo-generated with no gain. This usually corresponds well with the short circuit current, as long as extraction efficiency is good. In our case, we used  $V_{\text{ref}} = -1$  V, since at this bias, the photocurrent reached a plateau with slightly larger value than at short circuit. Current–voltage characteristics have been measured using a standard JV measurement setup and by pulsed measurements, both provided by a all-in-one measurement platform Arkeo (Cicci Research). In the pulsed mode, the device has been illuminated at each voltage by a white light emitting diode (LED) with pulses of 200 ms and a duty cycle of 50%. The  $I_{\text{light}}$  ( $I_{\text{dark}}$ ) current has been measured before switching off (on) the LED, taking the mean value over approximately 20 ms. Pulsed measurements have been performed in order to exclude that the observed effects are due to a slow transient during constant illumination.

The measurement data are presented in Fig. 2 (symbols). A small gain is observed, with consistent values between the two measurement methods. Around  $-5$  V, the device apparently shows breakdown behavior, which we ascribe to an increase in injection current induced by the electric field, as described in the following.

We have developed a phenomenological model in order to qualitatively reproduce reverse bias behavior and gain. Our model is based on the assumptions that current under small reverse bias is due to carrier injection from the  $\text{TiO}_2$  into the perovskite due to tunneling, similar to what has been proposed by Bowring *et al.*,<sup>18</sup> and that the electric

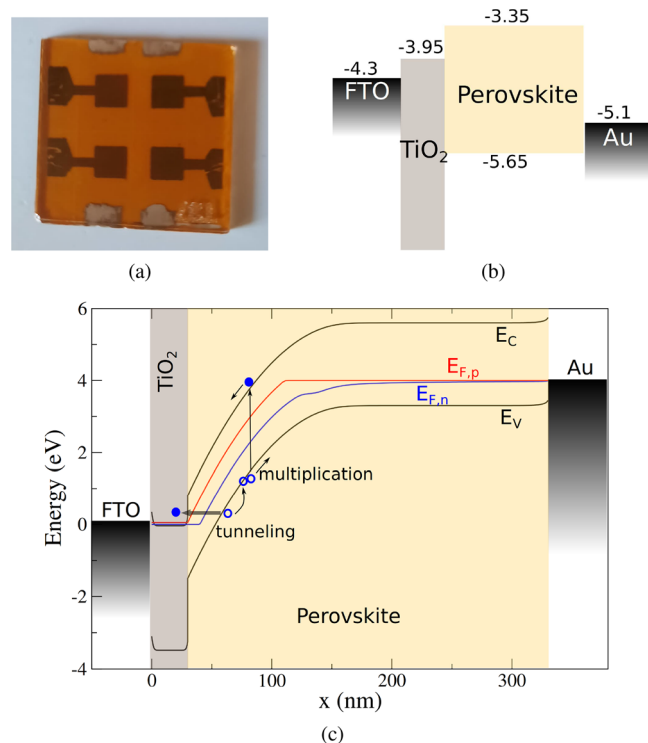


**FIG. 1.** Photograph of the studied mesoscopic device (a), material stack and energy alignment (b) and schematic figure of the proposed carrier injection processes (c). The band edge energies in eV used in the simulations are indicated in (b). The band profile in (c) is shown for  $-4$  V reverse bias in the dark. The band bending in the perovskite layer is due to the accumulation of positive charged mobile bromium vacancies ( $\text{V}_{\text{Br}}^+$ ) at the gold anode, which results in a negative background charge.

field in the perovskite layer can become sufficiently large to trigger carrier multiplication by impact ionization, as illustrated in Fig. 1(c). Tunneling-assisted carrier injection has been calculated numerically based on the band and quasi-Fermi level profiles, which have been obtained by solving the stationary drift-diffusion model,<sup>19</sup> including photo-generation, mobile ions, and avalanche multiplication.

It is commonly agreed that mobile ionic species in halide perovskite are playing an important role.<sup>20–22</sup> To account for the effects due to bias-induced ion accumulation on the potential profile, we explicitly included ionic species in the model. We assumed that only positively charged bromium vacancies ( $\text{V}_{\text{Br}}^+$ ) are mobile such that they accumulate at the perovskite/Au interface, while the band bending near the interface with the electron transport layer (ETL) is determined by a fixed negative background charge density, which compensates the total amount of  $\text{V}_{\text{Br}}^+$ .<sup>18</sup> In fact, under our model assumptions, the presence of mobile ions and their rearrangement due to the increased external field at negative bias is crucial for the reverse bias behavior. To determine the band profile, we explicitly include the ETL in the drift-diffusion simulation because it can affect the electric field in the perovskite layer and modify the carrier injection.

For the photo-generation profile, we used results from optical simulations for solar cells of similar structure,<sup>17</sup> adjusting the intensity

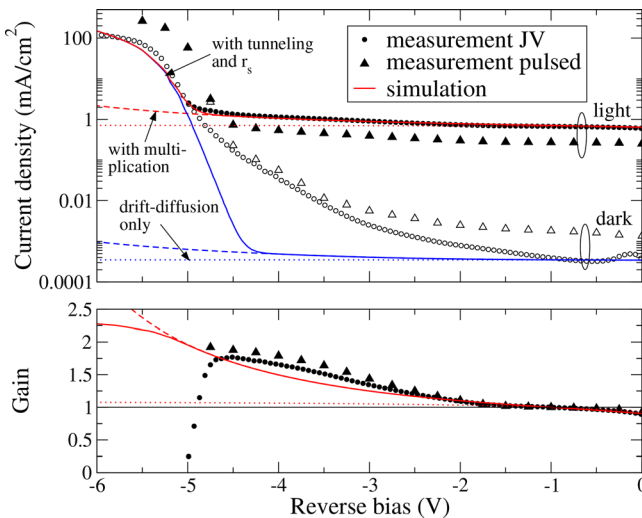


**FIG. 2.** Comparison between measured JV characteristics in the dark and under illumination with the model results. The simulation results have been obtained for a mean vacancy density of  $V_{Br} = 7.5 \times 10^{17} \text{ cm}^{-3}$ , and adding a series resistance of  $4 \Omega \text{ cm}^2$ . For comparison, we report also the characteristics from pulsed measurements. The lower panel shows the gain, calculated according to Eq. (1). Symbols show measured data, colored lines are simulation results. The dotted lines are obtained without including multiplication and tunneling, the dashed lines including only multiplication, and full lines are for the complete model.

such as to reproduce the measured short circuit current. The small dark current at low reverse bias has been added empirically to the model as a constant generation at the  $\text{TiO}_2/\text{MAPbBr}_3$  interface. Since its value does not considerably change between different devices with different or even absent hole transport layer (see Fig. 5 in [supplementary material](#)), we tentatively assign it to a trap assisted generation at the  $\text{MAPbBr}_3/\text{TiO}_2$  interface, enhanced possibly by the large interface area in the mesoporous layer. We assume the dominant recombination process at the light intensities used during the measurements (0.1–1 sun) to be interface recombination,<sup>21,23</sup> and a carrier recombination velocity of  $10^6 \text{ cm/s}$  has been added at the gold/MAPbBr<sub>3</sub> interface, in order to model the reduced extraction efficiency in cells without the hole transport layer.

For the avalanche generation, we used the standard model<sup>13</sup>

$$G_{av} = \alpha_n |j_n| + \alpha_p |j_p|, \quad (2)$$

where  $G_{av}$  is the resulting generation rate of electron-hole pairs in  $\text{cm}^{-3} \text{ s}^{-1}$  and  $|j_{n,p}|$  are the moduli of the electron and hole fluxes in  $\text{cm}^{-2} \text{ s}^{-1}$ . The impact-ionization rate coefficients  $\alpha_n$  and  $\alpha_p$  are strongly field dependent, and different models exist for them. We have used the Chynoweth law<sup>13</sup> given by  $\alpha_{n,p} = a_{n,p} e^{-b_{n,p}/F(x)}$ , where  $F(x)$  is the local electric field strength. Since neither experimental nor theoretical data are available on impact ionization and avalanche multiplication in lead-halide perovskites, we tentatively used values similar to the ones of GaAs, being a direct semiconductor with bandgap in a similar energy range. After slight adjustments, the used values were  $a_n = a_p = 3 \times 10^6 \text{ cm}^{-1}$  and  $b_n = b_p = 2.4 \times 10^6 \text{ V/cm}$ .

The total device current has finally been calculated by adding a tunnel-assisted injection current, which has been evaluated using the

simulated band profile. The model is based on band-to-band tunneling, assuming that electrons from the  $\text{MAPbBr}_3$  valence band can tunnel to the conduction band or directly to the  $\text{TiO}_2$ . The current is calculated as<sup>24,25</sup>

$$\begin{aligned} J &= -\frac{q}{\pi\hbar} \int \frac{d\mathbf{k}_\perp^2}{(2\pi)^2} \int_{E_{min}}^{E_{max}} dE T(E, \mathbf{k}_\perp) [f_L(E) - f_R(E)] \\ &\approx \frac{q}{\pi\hbar} \int_{E_{C,min}}^{E_{V,max}} dE \int \frac{d\mathbf{k}_\perp^2}{(2\pi)^2} T(E, \mathbf{k}_\perp). \end{aligned} \quad (3)$$

Here, we have assumed that the electron occupation in the valence band is  $f_R \approx 1$  and in the conduction band and  $\text{TiO}_2$  it is  $f_L \approx 0$ , according to the calculated quasi-Fermi levels. The integration in energy goes from the conduction band energy in the  $\text{TiO}_2$  to the maximum valence band energy. For the transmission function  $T(E, \mathbf{k}_\perp)$ , we used the WKB approximation with complex wave-vector from a two-band  $k \cdot p$  model.<sup>25</sup> Effective masses have been taken from the literature.<sup>26</sup>

To qualitatively reproduce the measured JV characteristics, we adjusted the amount of bromium vacancies in the simulation, and we added an additional external series resistance of  $r_s = 4 \Omega \text{ cm}^2$  in order to fit the linear part of the JV curve at large bias. Moreover, we assumed n-type doping in the ETL with a density of  $5 \times 10^{19} \text{ cm}^{-3}$ . All parameters are reported in Table 1 of the [supplementary material](#).

Figure 2 shows the experimental JV characteristics, measured as described above, together with the model results. The dotted curves are simulation results without avalanche multiplication and tunnel-assisted injection, while the dashed lines include avalanche multiplication and the continuous lines also tunnel-assisted injection. Note the slight increase in photo-generated current even without multiplication, which is due to the effect of electron recombination at the gold anode. The gain predicted by the model is compatible with the measured gain, which remains below 2 for this device. Note that above  $\sim 4.5 \text{ V}$ , the experimental extraction of gain is hampered by the large current component of injection from the  $\text{TiO}_2$ . The simplified model cannot predict the drop in gain, because the tunneling current is added *a posteriori* to the current obtained from the drift-diffusion simulation, which does, therefore, not influence  $I_{light} - I_{dark}$ .

The simulation results have been obtained assuming a mean bromium vacancy density of  $7.5 \times 10^{17} \text{ cm}^{-3}$ . This value is at the higher end of what has been reported in the literature.<sup>27</sup> The discrepancy in the dark current may be due to additional current contributions, e.g., due to electronic traps near the  $\text{TiO}_2/\text{MAPbBr}_3$  interface. The difference in breakdown voltage between the two measurement methods can be attributed to differences in charge distribution, for example, due to different measurement times. A slightly larger mean vacancy density of  $8 \times 10^{17} \text{ cm}^{-3}$  shifts the breakdown to the measured value and slightly increases gain, too.

In Fig. 3, we show the band profiles, electric field distribution, the avalanche generation rate, and electron and hole current densities obtained from the simulations for two different reverse bias voltages of  $-1$  and  $-4.5 \text{ V}$ . For comparison, the photogeneration current as the cumulative integral of the generation rate is also reported in the lowest panel. It can be observed that under the hypotheses of our model with the increasing negative bias, the region with large electric field grows, so that avalanche generation is predicted over an increasing distance and with an increasing rate. From the carrier current densities, it is

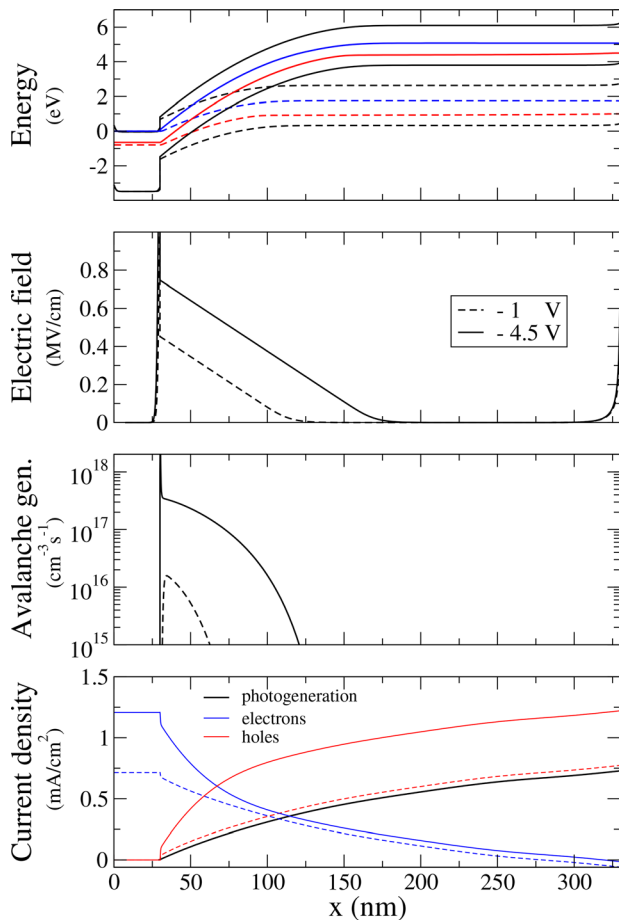


**FIG. 3.** The band profiles, electric field strengths, avalanche generation rates, and electron and hole currents at two different reverse bias voltages of  $-1\text{ V}$  (dashed lines) and  $-4.5\text{ V}$  (solid lines). The blue and red lines in the top panel show the electron and hole quasi-Fermi levels obtained from the standard drift-diffusion simulation, respectively. The black curve in the bottom panel is the cumulative photogenerated current. The offset compared to the hole current is due to interface recombination at the gold contact.

seen that at  $-1\text{ V}$  multiplication is not relevant, as the hole current closely follows the photogeneration current. The offset between the two is due to interface recombination at the gold contact.

Since the change in photocurrent and, thus, gain is small, it could be argued that the observed effect is entirely due to a bias dependent extraction efficiency that is improving with the increasing reverse bias. However, extracting the absorbed photon to current efficiency (APCE) from the measured incident photon to current efficiency (IPCE), performed on the same device at different negative biases and corrected by the calculated absorption efficiency (see the [supplementary material](#), Fig. 2), results in values larger than 100% starting from bias between  $-4$  and  $-5\text{ V}$ , as shown in [Fig. 4](#). This suggests the presence of an internal gain mechanism, as assumed in our model. Note also that the increase in APCE from  $0\text{ V}$  to  $-4\text{ V}$  by a factor of  $\sim 2$  is compatible with the measured photocurrent gain in [Fig. 2](#).

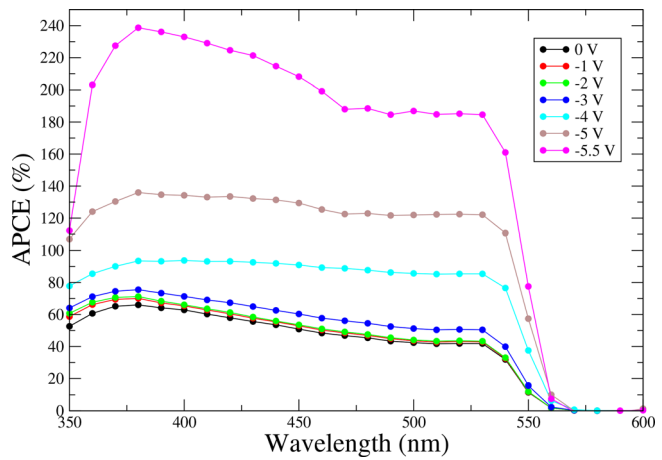


**FIG. 4.** APCE obtained from the measured IPCE, corrected with the simulated absorption efficiency, at different reverse bias. Between  $-4$  and  $-5\text{ V}$ , the APCE surpasses 100%, which indicates that the observed gain is not only due to improved carrier extraction. The data have been corrected for the dark current, which at higher bias is not negligible. Below  $350\text{ nm}$ , the measurement is affected by absorption in the Glass/FTO/TiO<sub>2</sub> layers.

An alternative explanation of the observed gain could be a change in the electric field due to illumination and, thus, in the tunneling rate. However, for our model parameters, the electric field changes negligibly with illumination, so that an additional ingredient to the model would be needed, e.g., trap states near the interface. However, a mechanism as described in Ref. 7 can be ruled out, since our devices behave as normal solar cells under forward and small reverse bias.

In conclusion, we have studied the reverse bias behavior of FTO/TiO<sub>2</sub>/MAPbBr<sub>3</sub>/Au devices, finding breakdown-like behavior at around  $-4\text{--}5\text{ V}$  and a small amount of photocurrent gain of  $\sim 2$ . Based on a phenomenological modeling strategy, we ascribe these tentatively to tunneling-assisted electron extraction at the TiO<sub>2</sub>/MAPbBr<sub>3</sub> interface and carrier multiplication, respectively. Both effects strongly depend on the electric field and, thus, on the density and spatial configuration of mobile ionic species. Increased extraction efficiency as sole origin of improved photocurrent has been excluded due to the observation of  $\text{IPCE} > 100\%$ , which suggests an internal gain mechanism. Alternative explanations for the observed gain cannot be excluded, though, which could, for example, involve trap-related processes or light-induced ionic transport. In particular, the role of mobile ions and interface traps needs further examination. A photoconductive effect, on the other hand, seems unlikely, since we would expect it to be observed also at small bias. Future studies also on MAPbBr<sub>3</sub> single crystals may hopefully provide more insight into both reverse bias breakdown and photocurrent gain in such detector devices.

See the [supplementary material](#) that provides the list of simulation parameters, the measured IPCE of two devices, the simulated photon absorption efficiency, and additional measured JV characteristics and gain for more devices.

The authors acknowledge financial support by the INFN group 5 and by the European Union's Horizon2020 research and

innovation program under Grant Agreement No. 826013 “IMPRESSIVE.”

## AUTHOR DECLARATIONS

### Conflict of Interest

The authors have no conflicts to disclose.

### DATA AVAILABILITY

The data that support the findings of this study are available from the corresponding author upon reasonable request.

## REFERENCES

- <sup>1</sup>Y. Zhao, C. Li, and L. Shen, “Recent advances on organic-inorganic hybrid perovskite photodetectors with fast response,” *InfoMat* **1**, 164–182 (2019).
- <sup>2</sup>J. H. J. Zhou, “Photodetectors based on organic-inorganic hybrid lead halide perovskites,” *Adv. Sci.* **5**, 1700256 (2018).
- <sup>3</sup>T. Moehl, J. H. Im, Y. H. Lee, K. Domanski, F. Giordano, S. M. Zakeeruddin, M. I. Dar, L.-P. Heiniger, M. K. Nazeeruddin, N.-G. Park, and M. Graetzel, “Strong photocurrent amplification in perovskite solar cells with a porous TiO<sub>2</sub> blocking layer under reverse bias,” *J. Phys. Chem. Lett.* **5**, 3931–3936 (2014).
- <sup>4</sup>X. Hu, X. Zhang, L. Liang, J. Bao, S. Li, W. Yang, and Y. Xie, “High-performance flexible broadband photodetector based on organolead halide perovskite,” *Adv. Funct. Mater.* **24**, 7373–7380 (2014).
- <sup>5</sup>Z. Lian, Q. Yan, Q. Lv, Y. Wang, L. Liu, L. Zhang, S. Pan, Q. Li, L. Wang, and J. Sun, “High-performance planar-type photodetector on (100) facet of MAPbI<sub>3</sub> single crystal,” *Sci. Rep.* **5**, 16563 (2015).
- <sup>6</sup>K. Domanski, W. Tress, T. Moehl, M. Saliba, M. K. Nazeeruddin, and M. Grätzel, “Working principles of perovskite photodetectors: Analyzing the interplay between photoconductivity and voltage-driven energy-level alignment,” *Adv. Funct. Mater.* **25**, 6936–6947 (2015).
- <sup>7</sup>R. Dong, Y. Fang, J. Chae, J. Dai, Z. Xiao, Q. Dong, Y. Yuan, A. Centrone, X. C. Zeng, and J. Huang, “High-gain and low-driving-voltage photodetectors based on organolead triiodide perovskites,” *Adv. Mater.* **27**, 1912–1918 (2015).
- <sup>8</sup>H. W. Chen, N. Sakai, A. K. Jena, Y. Sanehira, M. Ikegami, K. C. Ho, and T. Miyasaka, “A switchable high-sensitivity photodetecting and photovoltaic device with perovskite absorber,” *J. Phys. Chem. Lett.* **6**, 1773 (2015).
- <sup>9</sup>M. I. Saidaminov, M. A. Haque, M. Savoie, A. L. Abdelhady, N. Cho, I. Dursun, U. Buttner, E. Alarousu, T. Wu, and O. M. Bakr, “Perovskite photodetectors operating in both narrowband and broadband regimes,” *Adv. Mater.* **28**, 8144–8149 (2016).
- <sup>10</sup>Y. Zhang, Y. Liu, Y. Li, Z. Yang, and S. F. Liu, “Perovskite CH<sub>3</sub>NH<sub>3</sub>Pb(Br<sub>x</sub>I<sub>1-x</sub>)<sub>3</sub> single crystals with controlled composition for fine-tuned bandgap towards optimized optoelectronic applications,” *J. Mater. Chem. C* **4**, 9172–9178 (2016).
- <sup>11</sup>Y. Li, Z.-F. Shi, S. Li, L.-Z. Lei, H.-F. Ji, D. Wu, T.-T. Xu, Y.-T. Tian, and X.-J. Li, “High-performance perovskite photodetectors based on solution-processed all-inorganic CsPbBr<sub>3</sub> thin films,” *J. Mater. Chem. C* **5**, 8355–8360 (2017).
- <sup>12</sup>J. Song, Q. Cui, J. Li, J. Xu, Y. Wang, L. Xu, X. Jie, Y. Dong, T. Tian, H. Sun, and H. Zeng, “Ultralarge all-inorganic perovskite bulk single crystal for high-performance visible-infrared dual-modal photodetectors,” *Adv. Opt. Mater.* **5**, 1700157 (2017).
- <sup>13</sup>S. M. Sze and K. K. Ng, *Physics of Semiconductor Devices* (John Wiley & Sons, 2006).
- <sup>14</sup>C. de Weerd, L. Gomez, A. Capretti, D. M. Lebrun, E. Matsubara, J. Lin, M. Ashida, F. C. M. Spoor, L. D. A. Siebbeles, A. J. Houtepen, K. Suenaga, Y. Fujiwara, and T. Gregorkiewicz, “Efficient carrier multiplication in CsPbI<sub>3</sub> perovskite nanocrystals,” *Nat. Commun.* **9**, 4199 (2018).
- <sup>15</sup>E. Manousakis, “Optimizing the role of impact ionization in conventional insulators,” *Sci. Rep.* **9**, 20395 (2019).
- <sup>16</sup>Z. Xu, Y. Yu, S. Arya, I. A. Niaz, Y. Chen, Y. Lei, M. A. R. Miah, J. Zhou, A. C. Zhang, L. Yan, S. Xu, K. Nomura, and Y.-H. Lo, “Frequency- and power-dependent photoresponse of a perovskite photodetector down to the single-photon level,” *Nano Lett.* **20**, 2144–2151 (2020).
- <sup>17</sup>A. Singh, F. Matteocci, H. Zhu, D. Rossi, S. Mejaouri, S. Cacovich, M. Auf der Maur, F. Sauvage, A. Gagliardi, M. Grätzel, and A. D. Carlo, “Methylamine gas treatment affords improving semitransparency, efficiency, and stability of CH<sub>3</sub>NH<sub>3</sub>PbBr<sub>3</sub>-based perovskite solar cells,” *Sol. RRL* **5**, 2100277 (2021).
- <sup>18</sup>A. R. Bowring, L. Bertoluzzi, B. C. O’Regan, and M. D. McGehee, “Reverse bias behavior of halide perovskite solar cells,” *Adv. Energy Mater.* **8**, 1702365 (2018).
- <sup>19</sup>D. Rossi, F. Santoni, M. Auf der Maur, and A. D. Carlo, “A multiparticle drift-diffusion model and its application to organic and inorganic electronic device simulation,” *IEEE Trans. Electron Devices* **66**, 2715–2722 (2019).
- <sup>20</sup>J. M. Azpiroz, E. Mosconi, J. Bisquert, and F. De Angelis, “Defect migration in methylammonium lead iodide and its role in perovskite solar cell operation,” *Energy Environ. Sci.* **8**, 2118–2127 (2015).
- <sup>21</sup>T. S. Sherkar, C. Momblona, L. Gil-Escríg, J. Ávila, M. Sessolo, H. J. Bolink, and L. J. A. Koster, “Recombination in perovskite solar cells: Significance of grain boundaries, interface traps, and defect ions,” *ACS Energy Lett.* **2**, 1214–1222 (2017).
- <sup>22</sup>Q. Dong, J. Mendes, L. Lei, D. Seyitliyev, L. Zhu, S. He, K. Gundogdu, and F. So, “Understanding the role of ion migration in the operation of perovskite light-emitting diodes by transient measurements,” *ACS Appl. Mater. Interfaces* **12**, 48845–48853 (2020).
- <sup>23</sup>D. Glowienka, D. Zhang, F. D. Giacomo, M. Najafi, S. Veenstra, J. Szymkowiak, and Y. Galagan, “Role of surface recombination in perovskite solar cells at the interface of HTL/CH<sub>3</sub>NH<sub>3</sub>PbI<sub>3</sub>,” *Nano Energy* **67**, 104186 (2020).
- <sup>24</sup>E. O. Kane, “Theory of tunneling,” *J. Appl. Phys.* **32**, 83–91 (1961).
- <sup>25</sup>A. Pan and C. O. Chui, “Modeling direct interband tunneling. I. Bulk semiconductors,” *J. Appl. Phys.* **116**, 054508 (2014).
- <sup>26</sup>Y. Chang, C. Park, and K. Matsuishi, “First-principles study of the structural and the electronic properties of the lead-halide-based inorganic-organic perovskites (CH<sub>3</sub>NH<sub>3</sub>)PbX<sub>3</sub> and CsPbX<sub>3</sub>(X = Cl, Br, I),” *J. Korean Phys. Soc.* **44**, 889–893 (2004).
- <sup>27</sup>M. Fischer, D. Kiermasch, L. Gil-Escríg, H. J. Bolink, V. Dyakonov, and K. Tvingstedt, “Assigning ionic properties in perovskite solar cells: A unifying transient simulation/experimental study,” *Sustainable Energy Fuels* **5**, 3578–3587 (2021).